Angular multiscale statistics of turbulence in a porous bed

4 authors:

Xiaoliang He
Oregon State University
4 PUBLICATIONS   **12** CITATIONS

SEE PROFILE

Sourabh Apte
Oregon State University
121 PUBLICATIONS   **1,602** CITATIONS

SEE PROFILE

Kai Schneider
Aix-Marseille Université
300 PUBLICATIONS   **3,259** CITATIONS

SEE PROFILE

Benjamin Kadoch
Aix-Marseille Université
38 PUBLICATIONS   **123** CITATIONS

SEE PROFILE

Some of the authors of this publication are also working on these related projects:

Project   Modeling dense sprays using modified Euler-Lagrange approach View project

Project   Adaptive Multirresolution View project

Angular multiscale statistics of turbulence in a porous bed

Xiaoliang He,[1] Sourabh Apte,[1,*] Kai Schneider,[2] and Benjamin Kadoch[3]

[1]*School of Mechanical, Industrial and Manufacturing Engineering, Oregon State University, Corvallis, Oregon 97331, USA*
[2]*Aix-Marseille Univ., CNRS, Centrale Marseille, I2M, Marseille, France*
[3]*Aix-Marseille Univ., CNRS, IUSTI, Marseille, France*

Direct numerical simulation of pore-scale turbulence is performed in a unit cell of a face-centered cubic lattice at three different pore Reynolds numbers (300, 500, and 1000). The pore-geometry gives rise to very low porosity resulting in rapid acceleration and deceleration of the flow in different regions. Eulerian statistics of mean velocity and turbulent kinetic energy are first described to provide a good understanding of the overall flow topology. In addition, the spatial variances and probability density functions for the instantaneous and temporal fluctuation velocities are computed to assess the higher-order statistics. The flow field is then analyzed using angular Lagrangian multiscale statistics of fluid particles to study their directional change at different timescales. Two power laws are observed for the evolution of the mean absolute angle as a function of time lag, demarking the early time and an intermediate, inertial range. The effect of the geometric confinement on the asymptotic behavior of the angular statistics is examined in detail. An asymptotic limit different than $\pi/2$ (corresponding to equidistribution of the mean angle, observed for three-dimensional isotropic turbulence with periodic boundaries) or $\frac{2}{3}\pi$ (observed for two-dimensional wall-bounded turbulence) is obtained, representing the strong effect of geometric confinement on turbulence. Besides, the probability density functions (PDFs) for the instantaneous curvature angles are computed and the normalized PDFs are fit to a Fisher distribution. Furthermore, a Monte Carlo-based stochastic model is developed to predict the asymptotic curvature angle.

I. INTRODUCTION

Packed bed reactors are routinely used for synthesis of basic chemicals and intermediates in the chemical and process industries; e.g., packed-bed catalysis (Refs. [1,2]), as well as in the nuclear applications; e.g., high-temperature reactor (HTR) cooling (Ref. [3]). Random packing of porous media is one of the arrangements used in practice that exhibit typical flow Reynolds number on the order of 1000 or more. This results in unsteady inertial flows as well as transitional or even fully developed turbulence within pore space. Contrary to conventional thought about low-speed fluid flow in porous media, the inertial contribution to the flow field is often important in applications, and the inertial terms can dramatically change the topology of the flow field (such as formation of jets, vortices, dead zones, etc. within pores). These flow characteristics together with resultant dispersion properties play a critical role in the transport of reactants and products to and from active reaction sites. However, the mechanisms of how inertial and turbulent flows affect the macroscopic quantities, such as friction factor or pressure drop, are poorly understood (Ref. [4]).

---

*Sourabh.Apte@oregonstate.edu

Dybbs and Edwards [5] used direct observations using index-matched porous media to report on the topological characteristics of the microscale of the flow fields in the inertial range. They identified four distinct regimes for flow through porous media based on the pore Reynolds number (Re_p) defined as

$$\mathrm{Re}_p = \frac{U_{\mathrm{int}} D_B}{\nu_\gamma} \frac{\phi}{1-\phi}, \tag{1}$$

where U_{int} is the interstitial velocity of flow in porous media, D_B the bead diameter, ν_γ the kinematic viscosity of fluid, and ϕ is the porosity. The flow regimes are described below:

(1) Darcy or creeping flow regime, $\mathrm{Re}_p < 10$: Under these conditions, the flow is dominated by viscous forces. The drag force, however, makes little inertial contribution, which is proportional to the square of the Reynolds number [6]. It should be noted here that, although the flows are simple in this regime, much attention has been received from different perspectives of theory, experiment, and computation on this flow regime.

(2) The steady inertial (nonlinear) flow regime, $10 < \mathrm{Re}_p < 150$: A dramatic change in the character of the flow has been observed to occur in this regime as inertial forces begin to dominate over viscous ones [7,8]. The influence of the inertial term on the resulting flow field in porous media is similar in many ways to the secondary flows that have been reported by Taylor and others for curved tubes [9,10]. Helical and other complex flows have been observed experimentally [7] and predicted numerically [6,11–14] in simple periodic media at these Reynolds numbers.

(3) Unsteady laminar flow regime, $150 < \mathrm{Re}_p < 350$: In this regime, the flow is no longer steady [11], but it is not yet truly turbulent. Magnico [15] pointed out that increases in Reynolds number toward large enough values result in steady helical vortices in the form of tubes. Koch and Ladd [12] present 2D numerical simulations in a regular array of cylinders that exhibit quasi-periodic vortex shedding. Also, there have been direct experimental observations suggestive of vortex shedding (see Refs. [16–21]).

(4) The chaotic (fully developed turbulence) flow regime, $\mathrm{Re} > 350+$: Direct and indirect evidence of subpore-scale turbulence in porous media has been reported by several research groups [14,22–28]. There is some inconsistency among the groups, with some reporting turbulent conditions occurring at relatively low Reynolds numbers ($\mathrm{Re} \sim 350+$), whereas others have reported that turbulence was not observed till higher Reynolds numbers ($\mathrm{Re} \sim 1000$). The disparity among diverse publications probably represents differences in the geometry of the system under investigation and of the definition of turbulence.

Nearly all theoretical studies of dispersion in porous media have been on the condition of either (i) Stokes flow (which neglects the influence of inertial contributions completely), or (ii) inertial flow without any turbulence effects. Researchers typically rely on established empirical correlations for predicting transport and dispersive properties of flow in fixed beds and ultimately in reactor design [29,30]. Development of Reynolds-averaged Navier-Stokes (RANS) models for flow at the pore-scale level has been attempted by many researchers (for instance, in Refs. [31,32]). To name a few, the RANS k-ϵ model has been derived by time averaging the volume-averaged extended Darcy-Forchheimer model equations [33], or by volume averaging the time-averaged Reynolds-averaged equation [34–36], or by the double-decomposition technique developed based on exchangeability of volume-time or time-volume averaging [37], or by modifying the Darcy-Forchheimer model [32]. In these models, extra terms requiring closure are obtained by conducting numerical experiments using simple geometries such as a periodic array of rods and by using standard turbulence closure techniques based on a gradient diffusion hypothesis. However, these models lack validation with experimental or DNS data. A majority of these models predict nonzero Reynolds stress for laminar flows [38], making them inconsistent for applications over the full range of Re from laminar to turbulent flows.

Detailed, index-matched PIV data of turbulence in complex geometries of porous bed are difficult to obtain and very rare. Recently, Refs. [23,24] measured the turbulent flow field up to $\mathrm{Re}_p = 4000$

using the two-component PIV method implementing the refractive index matching technique in a random packing bed; Ref. [25] used a similar way to estimate the turbulent filtration in porous media. However, this method lacks in obtaining all velocity components, pressure fluctuations, and complete three-dimensional spectral analysis of turbulence statistics.

Obtaining velocity and pressure data using high-fidelity, direct numerical simulations (DNS) to investigate three-dimensional flow in complex porous media is thus critical to further advance reduced-order models especially in the unsteady, inertial as well as transitional and fully turbulent regimes. Some numerical works have been performed using the Lattice-Boltzmann method [22] for weakly turbulent and chaotic flow in a periodic porous medium, direct numerical simulations [27,28,39] for fully turbulent flows through packed beds, as well as large-eddy simulations [40].

Since the last decade, much attention has been drawn to the quantification of Lagrangian statistics [41] in turbulence. Lagrangian description of turbulence has unique physical advantages that are specifically important for mixing and dispersion studies in addition to the Eulerian statistics. The structural description of the statistical dynamics of turbulence is well captured by studying the temporal correlations along fluid particle trajectories compared to that from the investigation of spatial correlations of instantaneous velocity fields. Curvature of the flow trajectories (for example, Refs. [42–45]) is dominated by the small-scale structures and velocity gradients; but contains only little information on multiscale dynamics of turbulent flows. Some insights into the multiscale dynamics can be obtained from the standard Lagrangian structure functions; however, those then lack any direct information about the curvature of the flow. Bos *et al.* [46] and Kadoch *et al.* [47] introduced a new approach to study the trajectory of a fluid particle by computing the geometrical multiscale statistics. The curvature angle was defined by three adjacent points along a trajectory as a function of the time lag. Its evolution with respect to time increments was computed for both 3D isotropic turbulence and 2D forced turbulence with solid boundaries. For short time lags, the instantaneous angle is directly related to the curvature and is found to vary linearly with the time lag. For large time lags, an asymptotic limit of $\pi/2$ is approached, corresponding to the equidistribution of the angle, for unconfined flows such as isotropic turbulence, owing to symmetry and equal probability of possible trajectories at long times. This asymptotic limit can be easily used to study effects of geometric confinement on turbulence and resultant particle trajectories, making these Lagrangian statistics well suited for flow through porous media. In addition, the variation of the angle varies between the short and long-time limits contains the signature of the multiscale dynamics of turbulent flow.

In the present work, direct numerical simulation (DNS) of pore-scale turbulence is performed in a unit cell of a face-centered cubic lattice at three different pore Reynolds numbers (300, 500, and 1000). The pore-geometry gives rise to very low porosity resulting in rapid acceleration and deceleration of the flow in different regions. Hill and Koch [22] studied the same geometry using the Lattice-Boltzmann method for flows up to a Reynolds number of 300. They investigated transition from steady inertial to weakly turbulent and chaotic flows within this configuration. Their investigation focused on quantifying the transition process as well identifying inertial vortical flow structures. In the present work, simulations are performed in the fully turbulent regime (with the lowest Reynolds number investigated being similar to that of the highest Reynolds number studied by Hill and Koch [22]). This allows not only to investigate whether the flow features observed in their study persist at higher Reynolds numbers, but also to quantify the effects of geometric confinement on the turbulent flow and long-time dispersion by studying the Lagrangian multiscale statistics. Additionally, a stochastic model using Monte Carlo simulations characterizing the porous geometry in three-dimensions is developed and shown to predict this confinement effect on the asymptotic behavior of the curvature angle.

The rest of the paper is arranged in the following way. Section II provides the details of the porous geometry, simulation parameters, and the numerical approach. Section III presents the methodology for the angular Lagrangian multiscale statistics. Mean velocity field, TKE distributions, variances, and probability density functions for the instantaneous and temporal fluctuating velocities, Lagrangian correlations, energy spectrum, and the curvature angle statistics are described in Sec. IV. In addition,
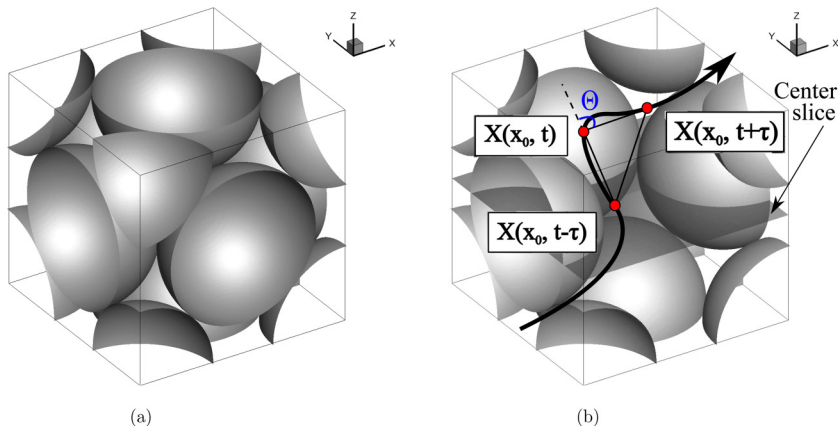
FIG. 1. (a) Schematic of a face-centered porous unit cubic cell; (b) same as (a) except some beads are removed and a particle trajectory illustrates the definition of the curvature angle Θ between subsequent Lagrangian particle increments.

a stochastic Monte Carlo-based model is developed which allows to predict the asymptotic behavior of the curvature angle in porous geometries. Finally, summary and conclusions are given in Sec. V.

II. SIMULATION SETUP

A. Porous geometry

A porous face-centered cubic (FCC) unit cell (Fig. 1) is used in this work. It has a half sphere entering at each face of the cube, and a half-quarter sphere at each corner. The face-centered cubic arrangement creates the lowest possible porosity (ϕ), the ratio of the void volume (V_{void}) to the total volume (V_{total}), to be 0.26 for the structured packings. Due to this extreme compactness, the flow through the unit cell experiences rapid expansion and contraction. A pressure gradient is imposed to drive the flow through the bed and a triply periodic boundary condition is applied for the unit cell. Majority of the flow enters the cubic cell through the upstream open corners, converges into the center pore resulting in strong accelerations and decelerations, and then leaving the unit cell along downstream corners.

Hill and Koch [22] studied the same geometry using the Lattice-Boltzmann method for flows up to $\text{Re}_p = 300$, where the pore Reynolds number (Re_p) is defined with the adoption of porosity as given in Eq. (1). In this work, the flow at three pore Reynolds numbers, $\text{Re}_p = 300$, 500, and 1000, is simulated using direct numerical simulation, ranging from unsteady inertial to turbulent regions. Note that the definition for Reynolds number used by Hill and Koch [22] is different from the one used in the present work. In Hill and Koch [22], Re is defined as

$$\text{Re} = \frac{\overline{U}_x \, a}{\nu_\gamma}. \tag{2}$$

where, $\overline{U}_x$ is the spatial averaged velocity component in the x direction, which is the superficial velocity and can be related with the interstitial velocity by $\overline{U}_x = U_{\text{int}}\phi$, and a is the radius of the bead. While in the current study, the pore Reynolds number Re_p is used as it includes the porosity (ϕ) and thus is more commonly used in porous media literature. To be consistent, Re mentioned in Hill and Koch [22] has been converted to Re_p in the current study. As a result, the highest Reynolds number Hill and Koch [22] used based on their definition is 106, which corresponds to Re_p of almost 300.

B. Numerical approach and grid convergence

The numerical approach is based on a fictitious domain method to handle arbitrarily shaped immersed objects without requiring the need for body-fitted grids [48]. Uniform Cartesian grids are used in the entire simulation domain, including both fluid and solid phases. An additional body force is imposed on the solid part to enforce the rigidity constraint and satisfy the no-slip boundary condition. The absence of highly skewed unstructured mesh at the bead surface has been shown to accelerate the convergence and lower the uncertainty [26]. The following governing equations are solved over the entire domain, including the region within the solid bed, and a rigidity constraint force, $\mathbf{f}$, is applied that is nonzero only in the solid region.

The governing equations read as

$$\mathbf{\nabla} \cdot \mathbf{u} = 0, \tag{3}$$

$$\rho_\gamma \left[\frac{\partial \mathbf{u}}{\partial t} + (\mathbf{u} \cdot \mathbf{\nabla})\mathbf{u} \right] = -\mathbf{\nabla} p + \mu_\gamma \nabla^2 \mathbf{u} + \rho_\gamma \mathbf{g} + \mathbf{f}, \tag{4}$$

where $\mathbf{u}$ is the velocity vector (with components given by $\mathbf{u} = (u_x, u_y, u_z)$, ρ_γ the fluid density, μ_γ the fluid dynamic viscosity, p the pressure, and $\mathbf{g}$ the gravitational acceleration.

A fully parallel, structured, collocated grid solver has been developed and thoroughly verified and validated for a range of test cases including flow over a cylinder and sphere for different Reynolds numbers, flow over touching spheres at different orientations, flow developed by an oscillating cylinder, among others. In addition, the flow solver is validated by comparing the numerical predictions with PIV data for flow through a randomly oriented packed bed [49]. The details of the algorithm as well as very detailed verification and validation studies have been published elsewhere [48]. In addition, the solver was also used to perform direct one-to-one comparison with a body-fitted solver with known second-order accuracy for steady inertial, unsteady inertial, and turbulent flow through porous media [26]. The details of this comparison focused on issues such as grid resolution needed near the wall, issues related to touching spheres and contact points, quality of solution compared with the body-fitted solver, comparison with experimental work of Ref. [7] on flow through a packed array of half spheres, and establishing the grid resolution requirement per bead diameter for predicting the unsteady flow-field in packed porous beds within 5% uncertainty based on the grid convergence index (GCI). Turbulent flow at a pore Reynolds number of 600 was also computed in the same configuration and compared with the body-fitted approach to obtain very good predictive capability of the present fictitious domain solver. This same solver was also used to study turbulent flow in a randomly packed bed of 51 spheres capturing complex pore-scale flow features in agreement with published data (Refs. [26,50]).

For the present studies, the flow is driven by a pressure drop as a body force in a triple periodic domain. According to Hill and Koch [22], a constant pressure gradient $\mathbf{\nabla} P$, whose magnitude is proportional to the nondimensional body force F, is used to drive the flow,

$$|\mathbf{\nabla} P| = \frac{18 \, \mu_\gamma \, c \, U_{\text{int}}}{D_B^2} F, \tag{5}$$

where, μ_γ is the dynamic viscosity of the fluid and c the solid volume fraction, defined as $\frac{2}{3}\pi (D_B/L)^3$ (L is the length of the unit cube). The body force F changes with the pore Reynolds number according to the linear fit obtained by Hill and Koch [22] and is given as

$$F = 365 + 10.9 \left(\frac{1 - \phi}{2} \text{Re}_p \right) \quad (27 < \text{Re}_p < 216), \tag{6}$$

$$F = 462 + 9.85 \left(\frac{1 - \phi}{2} \text{Re}_p \right) \quad (\text{Re}_p \geqslant 216). \tag{7}$$

TABLE I. Comparison of the body force obtained from correlation (7) and that obtained from the shear stress on sphere surfaces to maintain same Reynolds numbers.

Re_p $\diagdown$ F	300	500	1000
Eq. (7) (Ref. [22])	1506	2284	4106
Present study	1575	2362	4198

As shown in Table I, *a posteriori* calculation of body force needed to balance the shear stress on the sphere surfaces for different Reynolds numbers exhibits a good agreement with the above correlation, even for the range of Reynolds numbers studied in the present work.

Using the pressure drop given in Eq. (5) and performing an overall momentum balance on the bed, one can estimate the wall shear stresses. If we neglect the form drag (assuming viscous drag dominates), the estimated wall stress (τ_w) is the maximum possible value for a given Re_p

$$\frac{\Delta P}{L} = \tau_w \left(\frac{1 - \phi}{\phi} \right) \frac{6}{D_B}; \quad \text{Friction velocity, } u_\tau = \sqrt{\frac{\tau_w}{\rho}} \approx 0.5 \| \langle U_{\text{int}} \rangle \|. \tag{8}$$

Requiring the first grid point to be within $y^+ = y u_\tau / \nu = 1$, this indicates that the distance of the first grid point normal to the sphere surface is given as $y \approx 2 D_B / \text{Re}_p$. Recently, Gunjal *et al.* [51] conducted Reynolds averaged Navier-Stokes simulations in face-centered cubic arrangements of packed spheres to show that the ratio of surface drag to total drag was on the order of 0.21 for Re_p up to 1000. Taking this factor into account, modifies the estimate for near-wall grid resolution for $\text{Re}_p = 1000$ to roughly 200 points in each direction per bead to completely resolve all scales. Note that this estimate is based on assuming all pressure drop to be equal to the viscous drag. This provides an overestimation of the resolution requirement.

To obtain a more direct estimate on grid resolution requirements in the present DNS simulations, 3D DNS studies were performed at $\text{Re}_p = 500, 1000$ in a unit cell of face-centered cubic spheres with systematic grid refinement study using 48, 64, 96, 112, 128, and 144 grid points per bead diameter D_B. A grid converged solution was obtained for first-order (mean flow) as well as second-order statistics (turbulent kinetic energy, TKE) for $\text{Re}_p = 500$ at a resolution of $D_B/96$. For $\text{Re}_p = 1000$, the mean flow converged at $D_B/144$, whereas TKE was showed small changes compared to coarser mesh. This indicates that for the high Re_p simulations of up to $\text{Re}_p = 1000$, a grid converged solution can be expected with a resolution of around $D_B/150$. To obtain a high resolution DNS study and provide sufficient resolution in the bead contact region, a refined grid based on $D_B/\delta = 250$ (δ is the grid resolution in one direction) was used to resolve the pore-scale flow structures, which results in 353^3 degrees of freedom for each case. Ref. [14] has performed a grid convergence study on the same geometry and concluded that the current grid resolution provides a good representation of the flow field. In wall units, δ^+ is estimated to be less than 1 for $\text{Re}_p = 300$, close to 1 for $\text{Re}_p = 500$ and about 2 for $\text{Re}_p = 1000$.

III. LAGRANGIAN ANGULAR MULTISCALE STATISTICS

A. Definition of the Lagrangian angular statistics

The geometric confinement effects on the flow structures have received much attention recently [47], particularly for turbulent flows in porous media [27,40]. Angular multiscale statistics of fluid particle trajectories [46] are obtained to quantify the effect of confinement on the flow from a Lagrangian point of view. Following a fluid particle in the Lagrangian frame, an angle, Θ, formed by consecutive particle locations [see Fig. 1(b)], as a function of time lag is related to the coarse-grained curvature of the fluid particle paths. To calculate this angle, three equal-time lag (τ) points along the trajectory are chosen, and the instantaneous curvature angle Θ is defined as the angle between two
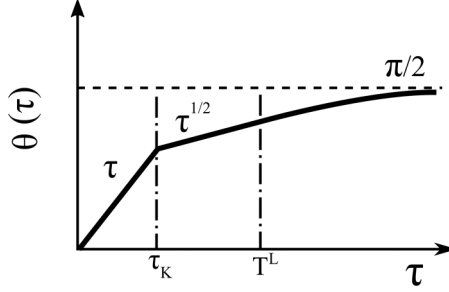
FIG. 2. Illustration of the two power laws and the asymptotic limit of the mean curvature angle θ evolution over time lags in log-log scale, where τ_K is the Kolmogorov timescale and T^L the integral timescale (reproduced according to Bos et al. [46]).

position vectors constructed consecutively by these three points using the following equation:

$$\cos(\Theta(t, \tau)) = \frac{\delta X(\mathbf{x}(t_0), t, \tau) \cdot \delta X(\mathbf{x}(t_0), t + \tau, \tau)}{|\delta X(\mathbf{x}(t_0), t, \tau)||\delta X(\mathbf{x}(t_0), t + \tau, \tau)|}, \tag{9}$$

where $\delta X(\mathbf{x}(t_0), t, \tau) = X(\mathbf{x}_0, t) - X(\mathbf{x}_0, t - \tau)$ is the spatial increment and $X(\mathbf{x}_0, t)$ is the position of a fluid particle at time t, which is initially injected at $\mathbf{x}_0$. The cosine of the angle describes the directional change of the particle with time lag and thus characterizes the multiscale feature of turbulent flows.

As discussed in Ref. [46], the major focus of the analyses will be on the average absolute angle

$$\theta(\tau) \equiv \langle |\Theta(t, \tau)| \rangle, \tag{10}$$

and the probability density functions (PDFs) of $\Theta(t, \tau)$. Two power laws and an asymptotic behavior are expected to characterize the evolution of the mean absolute angle as a function of time lag τ as illustrated in Fig. 2. At short time increments $(0 < \tau < \tau_K)$, the averaged angle is linearly proportional to the time lag with the constant of proportionality dependent on the curvature of the trajectory, corresponding to the ballistic regime, where the angle can be predicted by truncating the Taylor series expansion of the smooth trajectories under the conditions that both velocity and the perpendicular acceleration do not depend on τ. At intermediate times $(\tau_K < \tau < T^L)$, an inertial range is observed, especially for high Reynolds number flows, where the mean angle shows a linear trend with respect to the square root of τ. This can be explained using the Kolmogorov phenomenology, due to the fact that now the acceleration depends on τ. Thus, the inertial region is bounded by the Kolmogorov timescale (τ_K) and the integral timescale (T^L). At large time lags $(\tau \gg T^L)$, it has been shown in isotropic turbulence that the mean curvature angle approaches $\pi/2$, indicating that all directions are equally probable in the asymptotic limit. It is hypothesized that this evolution of the mean curvature angle may change in the presence of wall (solid surfaces of beads) confinement, owing to the limited directions that a fluid particle can traverse. Reference [47] has shown that in a confined two-dimensional turbulent flow field, the geometric confinement does have impact on the directional change of fluid particles and the asymptotic limit angle was found to be $\frac{2}{3}\pi$. In this work, this hypothesis is being tested in the three-dimensional turbulence field inside of a porous cubic cell. The asymptotic average absolute angle is determined to quantify the effect of confinement. The evolution of $\cos(\theta)$ and the PDFs of $[1 - \cos(\Theta)]$ at three different Re_p are compared to show the influence of the Reynolds number.

B. Particle tracking algorithm

Each tracer particle is injected at the center of a control volume at t_0. The initial Lagrangian tracer location $X(\mathbf{x}_{cv}, t_0)$ is the same as $\mathbf{x}_{cv}$, the center coordinates of the control volume which contains the

tracer. In the following, X_0 is used to represent $X(\mathbf{x}_{cv}, t_0)$ for simplicity. The fluid velocity $\mathbf{u}_{cv}(t_0)$ at corresponding $\mathbf{x}_{cv}$ is used as particle velocity $\mathbf{v}(X_0, t_0)$ at the first time step to advance tracers. After the initial time step, the particle velocity $\mathbf{v}(X_0, t_i)$ is calculated using trilinear interpolation of the Eulerian velocity field $\mathbf{u}(t_i)$ to the particle location, and a fourth-order Runge-Kutta (RK4) scheme is implemented to advance the tracer locations in time.

In this study, 10,000 particles are randomly released at the same time and tracked to collect the trajectories. The lifetime of each tracer is about 10 times the Lagrangian integral timescale, which ensures that the multiscale features could be well captured.

IV. RESULTS AND DISCUSSION

In this section, the Eulerian statistics of the mean and rms (root mean square) velocity fields inside the pore are first described briefly. The statistics are used to estimate the integral length scales and their variation with increasing Reynolds number. In addition, the variance and probability density function of the instantaneous and fluctuation velocity fields over the entire computational domain are computed to contrast the trends with studies at lower Reynolds numbers conducted by Hill and Koch [22].

The Lagrangian statistics including auto-correlations, integral timescales, and energy spectra are described next for the three Reynolds numbers followed by the angular multiscale statistics. Finally, a Monte Carlo-based stochastic model is presented and applied to predict the asymptotic limit of the curvature angle for the present geometry.

A. Porous flow description

As described earlier in the simulation setup, the flow through the triply periodic domain is driven by a body force in the flow direction based on the correlations given by Eq. (7). After an initial transient, a stationary state is reached and the computation is continued for several flow through times (T_f) over which statistics are collected. T_f is defined as

$$T_f = \frac{L}{U_{\text{int}}}.$$ (11)

where L is the length of the unit cube. For each case, the flow was first computed for several flow through times to ensure that a stationary state has been reached. This is confirmed by monitoring the total kinetic energy in the domain, which starts out to be a large value and then decreases and remains more or less constant after an initial transient period. This initial transient period was about $130T_f$ for the lowest and about $80T_f$ for the largest Reynolds number studied. After a stationary state has been established, the computations were performed for additional $80T_f$ for each Reynolds number to collect flow statistics which was found to be large enough to obtain converged statistics.

The distribution of Eulerian statistics of mean and turbulence kinetic energy inside the pore is illustrated below. The compactness and confinement of the porous bed geometry gives rise to regions of intense acceleration and deceleration as the flow enters the central pore from corners and then leaves at the corners on the other end. To visualize the flow field, the contours for time-averaged velocity component in the streamwise direction and the turbulent kinetic energy distributions at the center slice of the XY plane [Fig. 1(b)] are plotted in Fig. 3.

The mean velocity field normalized by U_{int}, shown in Figs. 3(a), 3(c), and 3(e), illustrates an almost identical distribution for all Reynolds numbers. The mean flow enters the center pore from the left hand side corners and starts to accelerate due to the geometric confinement, then decelerates and leaves the pore by the corners at the right-hand side. The uniform pattern of mean velocity distribution indicates that the largest flow motion in the pore is solely determined by the geometry. Even if the mean flowfield for all three Reynolds number is very similar, the situation is quite different for TKE. Observing from Figs. 3(b), 3(d), and 3(f), the TKE distributions, normalized by U_{int}^2, are varying substantially with increasing Reynolds number. First, the amount of TKE magnifies largely under the
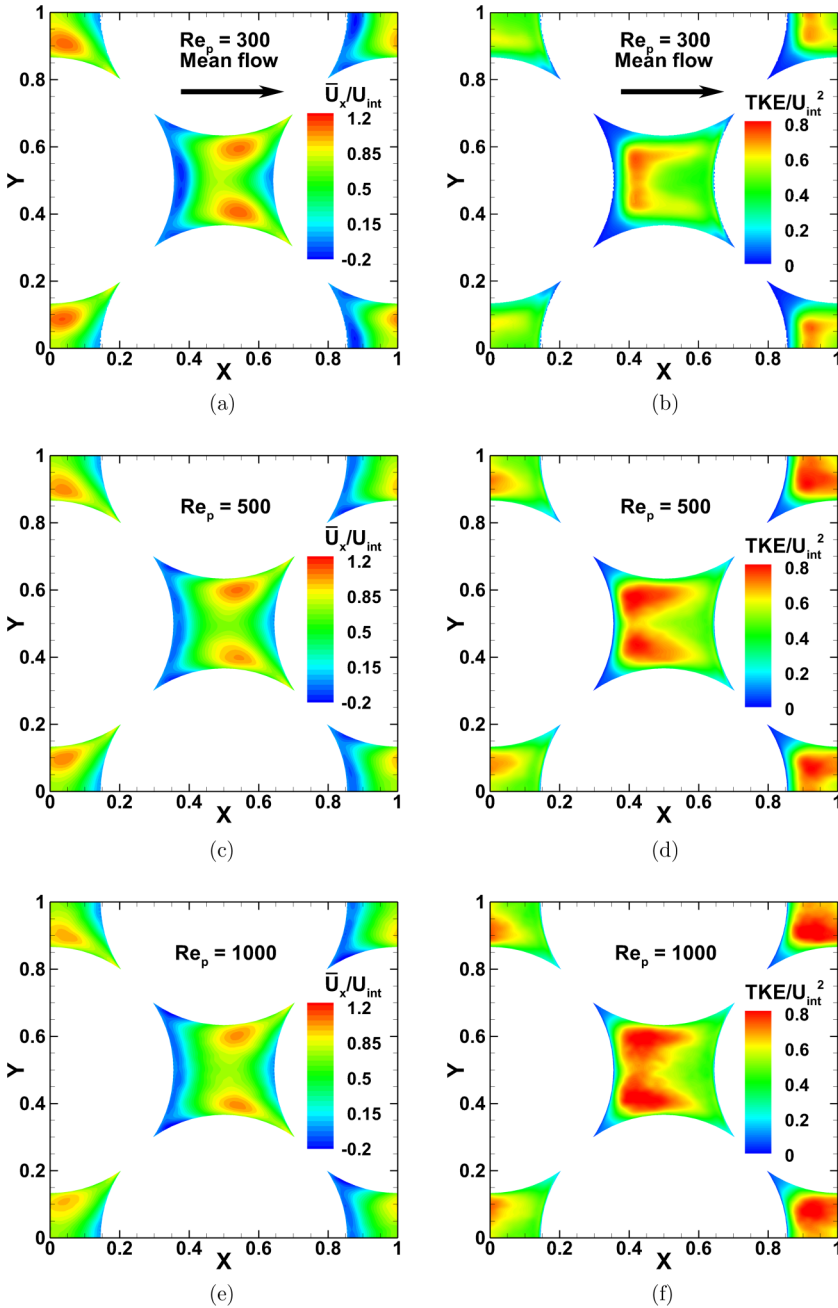
FIG. 3. Visualization of mean velocity in streamwise direction ($\overline{U}_x$) and TKE distributions at three Reynolds numbers. Top, $\mathrm{Re}_p = 300$; center, $\mathrm{Re}_p = 500$; bottom, $\mathrm{Re}_p = 1000$. The left side column shows velocity contour, and the right-hand side TKE.

effect of the stronger velocity fluctuations. Second, the distributions of TKE, although remaining in a semi-similar pattern, are moderately mutating with rising Re_p, especially in the center of the pore where the area with low TKE region is diminished apparently at higher Re_p. This is suggesting that the inertial term in the Navier-Stokes equation is playing an important role for higher Reynolds number

TABLE II. Time-averaged spatial variances of the instantaneous and temporal fluctuating velocities in the streamwise and spanwise directions at three different Reynolds numbers; the over bar means time-averaging; the first line are the data reported by Hill and Koch (2002) at the same Reynolds number of $\mathrm{Re}_p = 300$ at one time instant.

Re_p	$\overline{R}_{||}$	$\overline{R}_{\perp}$	$\overline{R}^f_{||}$	$\overline{R}^f_{\perp}$
300 by Ref. [22]	0.518	0.660	–	–
300	0.5546	0.7084	0.1440	0.1964
500	0.6125	0.7474	0.2218	0.2867
1000	0.6646	0.7758	0.2801	0.3500

flows in the porous media. To summarize, the mean velocity field, i.e., the large-scale motion, keeps the same distribution with increasing Reynolds number; while the generation of TKE, representing the small scale motions, is greatly enlarged and its distribution is noticeably altered. The multiscale nature of turbulence inside of porous bed is revealed by such visualizations.

B. Flow field statistics

To quantify the observations from the previous section, the statistics of the instantaneous velocity ($\mathbf{u}$) and the temporal fluctuating velocity ($\mathbf{u}'$) are investigated in detail by computing the spatial variance and the probability density functions at different Reynolds numbers. Similar to the temporal fluctuation velocity computed by using Reynolds-averaging,

$$\mathbf{u}' = \mathbf{u} - \overline{\mathbf{U}}, \tag{12}$$

where $\overline{\mathbf{U}}$ is the temporal average, the spatial fluctuation of any quantity ψ is defined by

$$\tilde{\psi} = \psi - \langle \psi \rangle^{\gamma}, \tag{13}$$

where $\tilde{\psi}$ is the spatial fluctuation of ψ, $\langle \rangle$ represents spatial averaging, and the superscribed γ indicates the averaging is performed in the fluid domain only. Hill and Koch [22] conducted a similar analysis for lower Reynolds numbers; however, their results were restricted to only the instantaneous velocity fields for the steady and weakly turbulent flow regimes. For the current study, the statistics, including the spatial PDFs and variances are first sampled in the fluid domain at multiple time instances over about $10T_f$, and then time-averaged.

1. Spatial variance

Following Hill and Koch [22], the spatial variance for instantaneous velocity is referred to as $\mathbf{R}$ and defined by

$$\mathbf{R}_{ij}(t) = \langle \tilde{u}_i \tilde{u}_j \rangle^{\gamma} / U^2_{\mathrm{int}}. \tag{14}$$

The streamwise and spanwise components of the variances are given by the diagonal part of $\mathbf{R}_{ij}$ as

$$R_{||} = \mathbf{R}_{11} \quad \text{and} \quad R_{\perp} = (\mathbf{R}_{22} + \mathbf{R}_{33})/2, \tag{15}$$

where the subscript $||$ represents streamwise and $\perp$ spanwise directions, respectively. For the temporal fluctuation velocity, the spatial variances in the streamwise and spanwise directions, i.e., $R^f_{||}$ and $R^f_{\perp}$, are defined in a similar way as Eqs. (14) and (15).

Table II shows the time-averaged spatial variances for the instantaneous and fluctuating velocities in both streamwise and spanwise directions. A reasonable agreement of the variances at $\mathrm{Re}_p = 300$
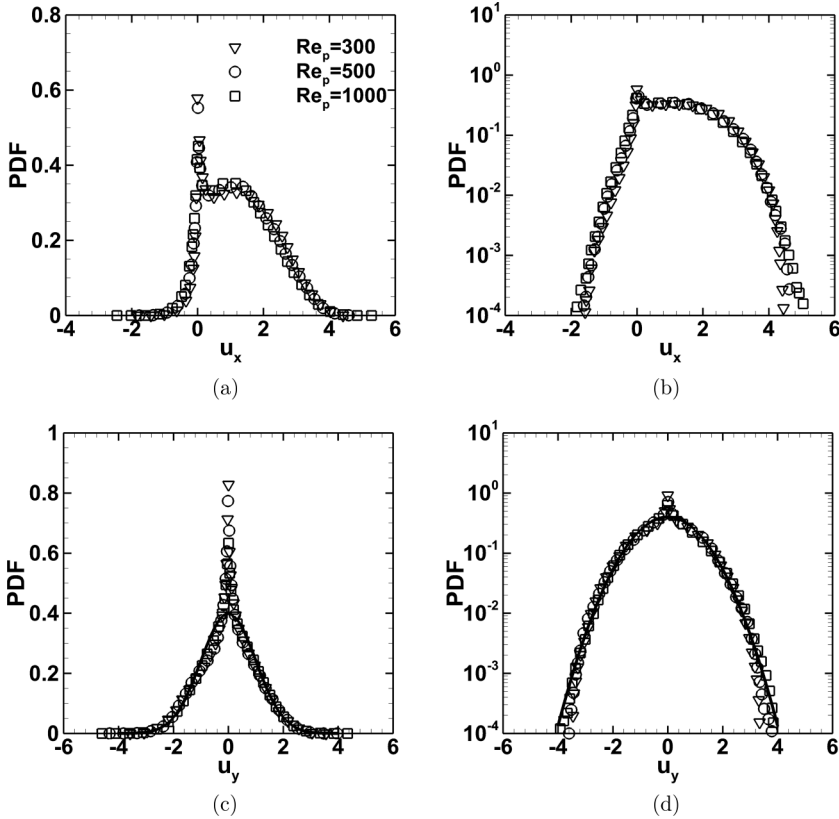
FIG. 4. PDFs of the instantaneous velocity component in *x* direction (a), and (b) showing the same data as (a) but in the lin-log scale; (c) and (d) are showing the velocity component in *y* direction, where the solid line represents the Gaussian distribution with zero mean and unit standard deviation.

is found between the current study and Hill and Koch [22]. The small differences may be attributed to (i) the time-averaging, which may have removed some of the temporal fluctuations, and (ii) the grid resolution, which was much coarser in Hill and Koch [22], so that some very small velocities near the solid wall may not be completely resolved in their work.

Observing from Table II, the variance of the instantaneous velocity is larger than that corresponding to the fluctuating velocity for all Reynolds numbers. In addition, the variance values in the streamwise direction are smaller than that in the spanwise directions. This is also confirmed by the PDFs in Fig. 4, as discussed further below, which shows that the instantaneous velocity in the streamwise direction has an asymmetric distribution with the tail on the left-hand side being much smaller than that on the right-hand side; while the PDF for velocity in the spanwise direction generally follows the Gaussian distribution. This is owing to the fact that the mean flow is strong in the streamwise direction, while almost zero in the other directions.

The variance of the temporal fluctuating velocity increases significantly with increasing Reynolds number. This indicates that the turbulence is more intensified, which is consistent with the observations from Figs. 3(b), 3(d), and 3(f). The spatial variances for the instantaneous velocity, however, in both streamwise and spanwise directions increase only slightly with respect to Reynolds number, which is consistent with the results reported in Hill and Koch [22]. The explanation is that the major part of the variances of instantaneous velocity components in a closely packed bed should come from the velocities near the bead surface, which essentially are very weak due to the no-slip boundary condition.
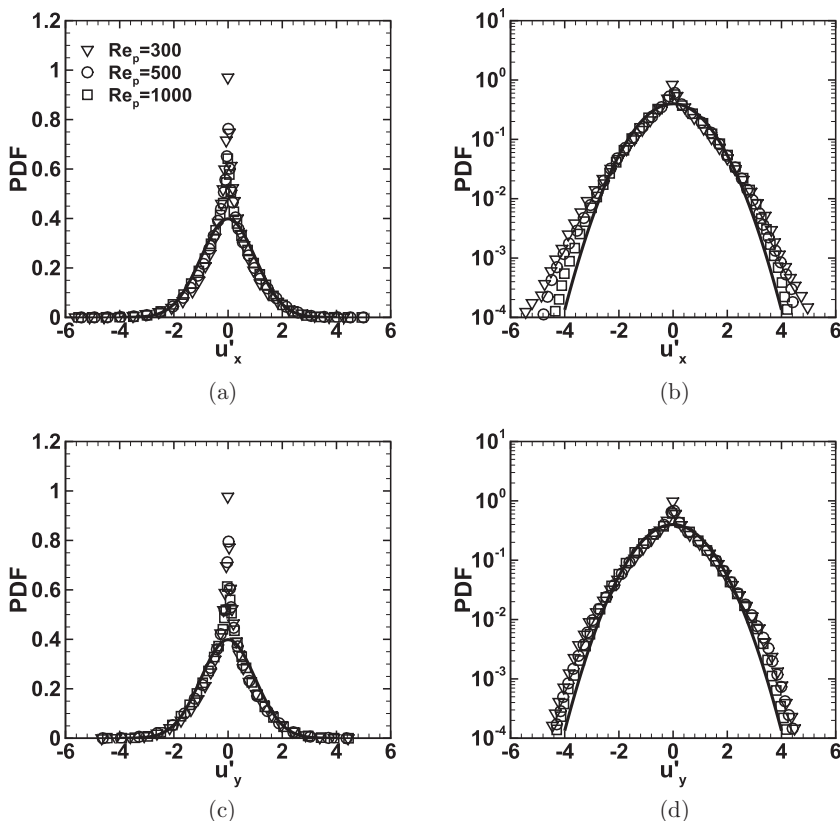
FIG. 5. The PDFs for fluctuating velocity components in x direction (a), and (b) showing the same data as (a) but in the lin-log scale; (c) and (d) are showing the velocity component in y direction, where the solid line represents the Gaussian distribution with zero mean and unit standard deviation.

2. Probability density function

The probability density functions for the instantaneous and temporal fluctuating velocities are provided in Figs. 4 and 5, respectively. The variances in Table II are used to normalize the PDFs so that they have unit standard deviations. Owing to the periodicity, the statistics in y and z directions should be the same (which was verified) and hence only the PDFs of velocity in y direction are shown. The figures on the right hand side column are showing the same data as on the left, except that they are plotted in the lin-log scale.

a. Instantaneous velocity. The PDFs for the instantaneous velocity components in the streamwise and spanwise directions are given in Fig. 4. One common feature of the PDFs for both velocity components in the streamwise and spanwise directions is the distinguished peak in the PDF at zero of abscissa. It is also observed that the corresponding probability decreases with increasing Reynolds number suggesting that at lower Reynolds numbers, there is higher probability for small values of velocity.

Close observation of Figs. 4(a) and 4(b) shows some similar trends as reported by Hill and Koch [22] for the velocity in the main flow direction (x direction). At higher Reynolds number, more x component velocities in the upstream direction are detected. This can be observed at the left tail of the PDFs, especially in Fig. 4(b). It is the result of stronger recirculation as well as due to large amount of vortices generated with one of the components perpendicular to the x direction. A secondary peak is detected at about 1.5 times the standard deviation [see Fig. 4(a)], and the corresponding probability

becomes higher for larger Reynolds numbers. These characteristics of the PDF are not as pronounced at the lower Reynolds number flows studied by Hill and Koch [22] and potentially result from the stronger fluctuations owing to unsteady inertial effects at higher Reynolds numbers. In addition, a near-exponential decay, at a rate faster than the Gaussian distribution, is observed at the right hand side tail of the PDFs, especially for lower Reynolds numbers; and the decay rate is closer to the Gaussian distribution at higher Reynolds numbers.

The PDFs of instantaneous velocities in the spanwise direction, shown in Figs. 4(c) and 4(d), are symmetric with a peak at the center. They decently follow the Gaussian distribution until about three times the standard deviation in both positive and negative abscissas. Then they continue to decay, but at a rate that is noticeably larger than the Gaussian case. Similar to what has been noted for the streamwise velocity, at lower Reynolds numbers, the decay rate is more likely an exponential function; while for higher Reynolds numbers it is closer to the Gaussian distribution. This shows that the decay rates of the tails of the velocity field are Reynolds number dependent for the range considered in the present study. Hill and Koch [22] conjectured that the exponential decay at lower Reynolds numbers is because of the distribution of the pore size and not dependent upon the Reynolds number. However, as shown in the present study, with increasing Reynolds numbers, the flow structures and length scales become smaller even in the main flow direction. This isotropization of the velocity field at higher Re_p is more clearly seen in the PDFs of the fluctuating velocity rather than the instantaneous velocity. At lower Reynolds numbers, the flow structures are elongated in the main flow direction, and give rise to larger fluctuating velocities.

b. Temporal fluctuating velocity. Figure 5 illustrates the PDFs for the temporal fluctuation velocity components in the streamwise and spanwise directions. Similar to Fig. 4, the figures on the right column are in linear-log scale showing the same data as those on the left.

It can be observed that, except the spikes at the center, the PDFs for the fluctuating velocity in both streamwise and spanwise directions follow the Gaussian distribution until about three standard deviations. After that, the PDFs fall down at rates slower than the Gaussian distribution, unlike the PDFs of instantaneous velocity. However, similar to the instantaneous velocity, the PDFs at higher Reynolds number are closer to the Gaussian distribution, whereas for lower Re_p, it follows an exponential decay. These are consistent with the hypothesis that with increasing Re_p, the length scales and flow structures in all directions become smaller thus decreasing the magnitude of fluctuations in velocity. In addition, distinct peaks are seen at the zero of the abscissa just like the instantaneous velocity and the value of the probability of the peaks decreases with increasing Re_p, indicating that the turbulence is greatly enhanced by the unsteady inertial effects. Moreover, an asymmetric distribution is detected from Figs. 5(a) and 5(b) for PDFs of velocity fluctuations in the main flow direction, whereas the PDFs are mostly symmetric for spanwise directions, as shown in Figs. 5(c) and 5(d).

C. Lagrangian auto-correlation and energy spectrum

Lagrangian statistics are more important in the sense of dispersion analysis for flow through porous media. According to Ref. [52], turbulent dispersion is easier to understand physically within the Lagrangian framework. In this section, fluid tracer particles are tracked to obtain the Lagrangian trajectories. Tracer trajectories are then used to calculate Lagrangian velocity auto-correlations and energy spectrum.

The Lagrangian auto-correlations are computed according to Eq. (16) [53],

$$\rho_{ij}^L(\tau) = \frac{\langle v_i'(X_0, t) \ v_j'(X_0, t + \tau) \rangle}{[\langle v_i'^2(X_0, t) \rangle \langle v_j'^2(X_0, t + \tau) \rangle]^{1/2}}, \tag{16}$$

where ρ_{ij}^L is the Lagrangian auto-correlation, v_i' the ith component of the particle fluctuation velocity and $\langle \rangle$ represents ensemble averaging. The results are plotted in Figs. 6(a)–6(c), where the abscissa, i.e., the time lag τ, is normalized by the corresponding Lagrangian integral timescale, T_{11}^L computed
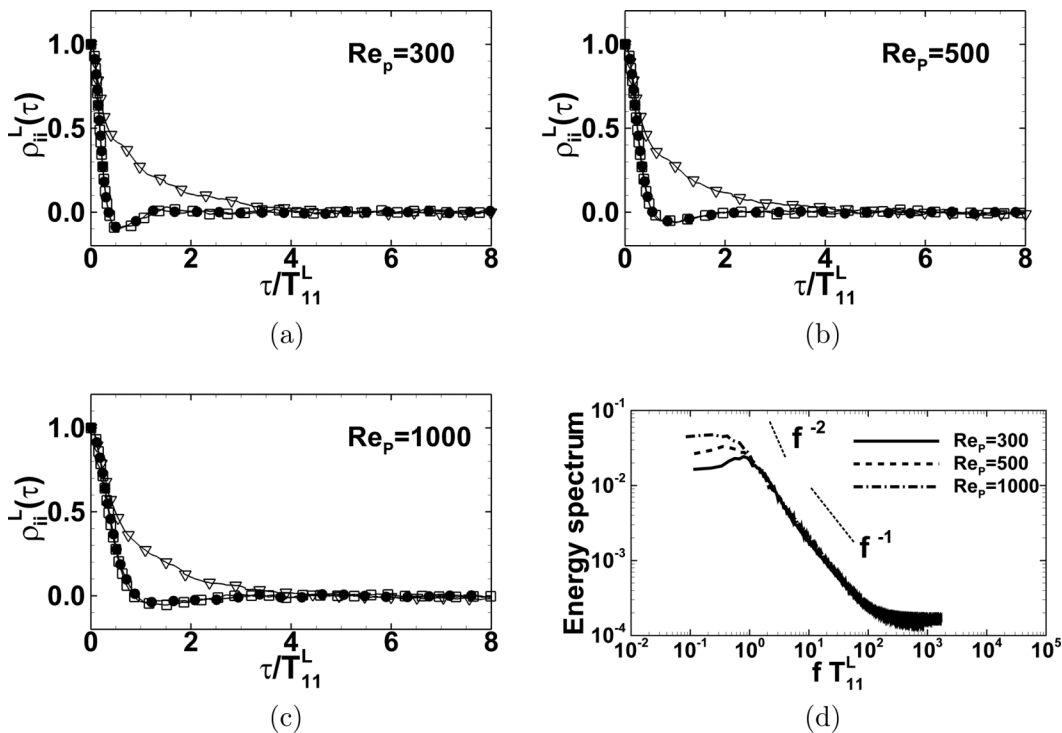
FIG. 6. Lagrangian auto-correlation with x axis normalized by the corresponding integral timescale T_{11}^L, (a) $\mathrm{Re}_p = 300$, (b) $\mathrm{Re}_p = 500$, and (c) $\mathrm{Re}_p = 1000$, where —▽— is ρ_{11}^L, —□— ρ_{22}^L, and —●— ρ_{33}^L; (d) energy spectrum of ρ_{11}^L for all three Reynolds numbers.

by integrating the auto-correlation over the abscissa as

$$T_{11}^L = \int \rho_{11}^L(\tau \geqslant 0)d\tau. \tag{17}$$

It is observed that the correlations in the spanwise directions decorrelate much faster than those in the streamwise direction regardless of the Reynolds number. Also, the correlation in the streamwise direction decorrelates at about four times of T_{11}^L monotonically. Since the integral timescale (T_{11}^L) decreases greatly with respect to Reynolds number, the correlations for the largest Reynolds number, $\mathrm{Re}_p = 1000$, fall down much quicker than the other two. The timescale separation in distinct flow directions and also for different Reynolds numbers characterize the multiscale nature of turbulence in porous bed.

Table III shows the normalized Eulerian integral length and Lagrangian integral timescales, obtained from the respective auto-correlations, for the three Reynolds numbers studied here. The integral length scale is scaled with the bead diameter (D_B). It is observed that even for the lower Re_p case, the integral length scale is only about 10% of the sphere diameter, indicating that the

TABLE III. Normalized integral length and timescales for different pore Reynolds numbers.

Re_p	300	500	1000
L_{11}^E/D_B	0.102	0.0884	0.0684
$(T_{11}^L U_{\mathrm{int}})/D_B$	0.55	0.356	0.322

coherent structures are confined within the pore. Such observation supports the pore scale prevalence hypothesis (PSPH) and the results reported in Jin *et al.* [28]. This implies that, the turbulence in the pore-scale is strongly affected by the porosity, and restrained by the pore size.

The integral timescale normalized by the flow timescale based on the interstitial velocity and the bead diameter is also given in Table III. Since the integral timescale is smaller than this flow timescale, this suggests that the Lagrangian coherent structures are restricted by the pore size. As a result, the single periodic unit cell considered in the present work appears to be sufficient for the Reynolds numbers studied. However, the timescale shows that for smaller Reynolds numbers the integral timescale approaches the flow timescale. Hence, for lower Reynolds numbers, larger computational domains may become necessary.

Additionally, Lagrangian energy spectra are computed by applying a Fourier transform to the auto-correlations in the streamwise direction and plotted in log-log scale in Fig. 6(d). The abscissa is the frequency f normalized by multiplying with the integral timescale. According to Ref. [54], the Lagrangian energy spectrum should follow a power law with an exponent close to -2, representing the inertial flow regime. Inspection of Fig. 6(d) shows that even for the highest Reynolds number the spectrum is only following a power law with slope of -2 in a very small region (around $f = 1$). For larger values of f, a pronounced f^{-1} behavior is observed. This is typical of energy spectra for the low Reynolds numbers studied here. Even $\text{Re}_p = 1000$ is not high enough to observe a wide inertial scaling in the Lagrangian energy spectrum. This is discussed with more details in the following section.

D. Lagrangian angular multiscale statistics

As mentioned in Sec. III, the Lagrangian tracer trajectories are used to compute the instantaneous curvature angle Θ by Eq. (9) to assess the influence of the confinement on the flow structures. Since the turbulent flow is in statistically stationary state, ensemble averaging is applied for all trajectories to obtain an overall representation of the mean angle θ. However, according to the previous results reported in Ref. [39], since the mean flow is very strong, the trajectories obtained using fluid particles advancing with instantaneous velocities $(\overline{\mathbf{U}} + \mathbf{u}')$ do not show the asymptotic behavior of the averaged angle. As a result, the particles are advanced using the fluctuation velocities $(\mathbf{u}')$ only to eliminate the mean flow effects. The evolution of the average absolute angle θ, characterizing the directional change of a particle, as a function of time lag is shown in Fig. 7(a) at three different Reynolds numbers.

The presence of two power laws is apparent. For short time lags, a ballistic regime is obtained regardless of Re_p. This linear behavior corresponds to smooth trajectories where particles have the tendency to go straight, which are generally independent of the flow geometry. However, in the inertial region, θ is expected to correlate with $\tau^{1/2}$, which becomes more heavily pronounced at higher Re_p, indicating its dependency on the Reynolds number. This trend is observed in Fig. 7(a) and the highest Reynolds number flow ($\text{Re}_P = 1000$) has a somewhat noticeable inertial region, while at $\text{Re}_p = 300$ it is barely seen. It should be noted that a significant scale separation, as observed in high Reynolds number turbulent flows, is not present. This is mainly because $\text{Re}_p = 1000$ is still not sufficiently large, and extending the study to even higher Reynolds numbers becomes computationally very expensive. The slow emergence of the inertial range in Lagrangian statistics is fairly common [46]. To see the extent of the inertial range, the inset of Fig. 7(a) shows the compensated angle, $\tilde{\theta}(\tau) = \theta(\tau)U_{\text{rms}}/(\epsilon\tau)^{1/2}$, where U_{rms} is the root-mean-square velocity, and ϵ is the total dissipation rate. It shows a plateau, which becomes more pronounced for $\text{Re}_p = 1000$.

The origins of these two power laws are discussed in Ref. [46]. Besides, the inertial region is also found to be bounded by the Kolmogorov timescale and integral timescale. More importantly, the asymptotic mean angle for all three Reynolds numbers collapse at the same value, 1.72 radian, which is noticeably higher than $\pi/2$ corresponding to equidistribution and obtained for isotropic turbulence [46]. It is conjectured to be connected with the porous bed arrangement. Also, because of the uniformity of the asymptotic mean angle for all cases, it can be hypothesized that the asymptotic
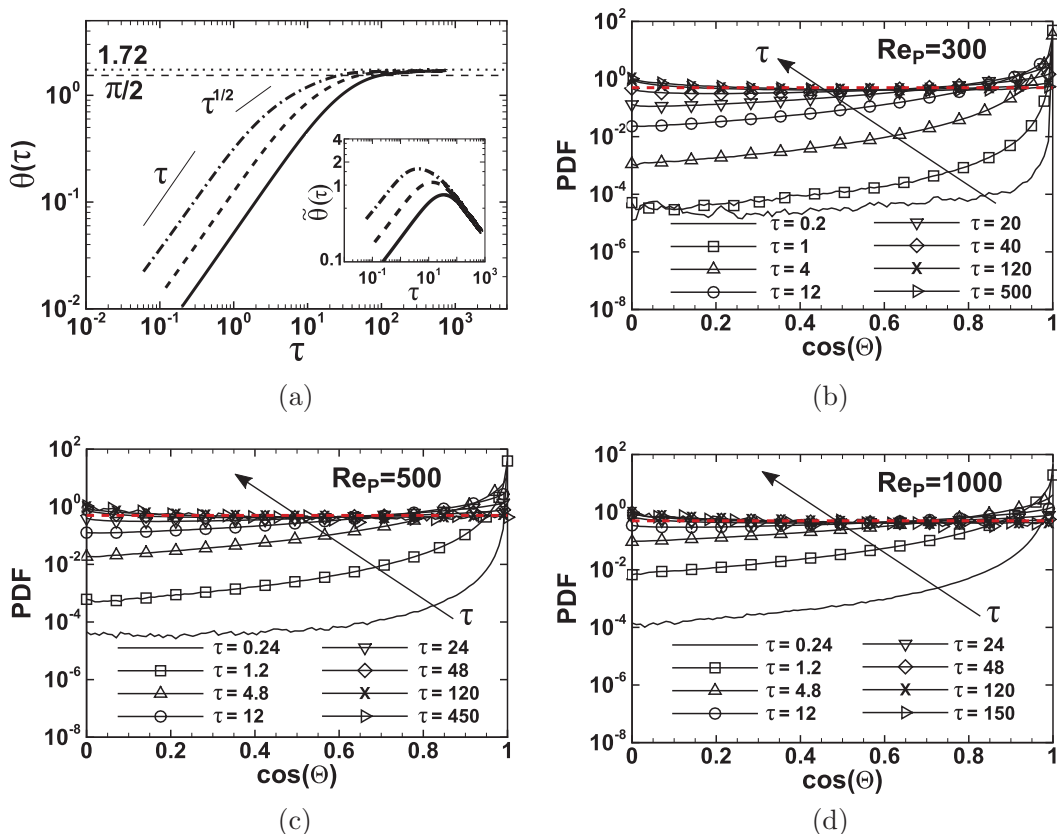
FIG. 7. (a) Evolution of the mean absolute angle θ for $Re_p = 300$ ———, $Re_p = 500$ ‑ ‑ ‑ ‑, and $Re_p = 1000$ ‑·‑·‑·‑; probability density functions for $\cos(\Theta)$, (b) $Re_p = 300$, (c) $Re_p = 500$, and (d) $Re_p = 1000$; the red dashed line ‑ ‑ ‑ ‑ ‑ denotes the value of uniform distribution, 0.5.

average angle θ is exclusively determined by the geometry. This hypothesis is further tested by developing a stochastic model that can predict this asymptotic behavior and the influence of the pore geometry, as discussed in Sec. IV E.

The above analyses are focusing on the mean absolute angle only. In the sense of the higher order statistics, the PDFs for the cosine of the instantaneous curvature angle $\cos(\Theta)$ and its evolution with time lag are plotted in Figs. 7(b), 7(c), and 7(d). For very short time increments, a spike near $\cos(\Theta) = 1$ can be observed for all Reynolds number cases, implying that the particles tend to move smoothly along the trajectory and have a pronounced tendency to go straight. For larger time lags, an equidistribution with the probability of $1/2$ (the red dashed line) is approached, i.e., the ballistic regime. This is coming from the fact that, the cosine of the angle generated by any pair of three randomly chosen points in the three-dimensional domain, which are decorrelated to each other due to the sufficiently long time interval, should be equidistributed (Ref. [46]). Also, the rate of PDFs transitioning from one peak near $\cos(\Theta) = 1$ to the equidistribution is believed to be related with the Reynolds number. As mentioned in Sec. IV C, the integral timescale decreases dramatically with increasing Re_p. This suggests that the faster decorrelation of the flow structures leads to an earlier transition to the equidistribution of the PDFs.

Additionally, according to Refs. [46,47], the PDFs for $\cos(\Theta)$ should be able to fit to a Fisher distribution under the assumption that velocity and acceleration are in near-Gaussian distribution and independent. From the PDFs shown in Fig. 5, it is observed that the spatial PDFs of fluctuation
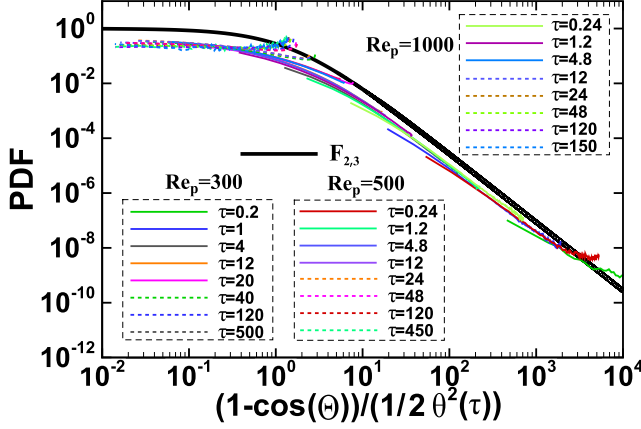
FIG. 8. PDFs of the normalized instantaneous curvature angle, short times in solid colored lines, long times in dashed color lines, and the bold black solid line represents the $F_{2,3}$ distribution.

velocities nearly follow the Gaussian distribution. If this assumption also holds for the acceleration, the squares of both velocity and acceleration should follow the χ^2 distribution, and the ratio of these two χ^2 distributed variables ought to comply with the Fisher distribution. As for Θ in the current study, its cosine can be approximated as $\cos(\Theta) \approx 1 - \Theta^2/2$ when the curvature angle is small. As a result, under such assumptions and using normalization, the PDFs of $1 - \cos(\Theta)$ are expected to align with the Fisher distribution. The results are plotted in Fig. 8, where all the PDFs displayed in Figs. 7(b)–7(d) are compiled together in colored lines and the $F_{2,3}$ distribution is shown as bold black solid line. The numbers 2 and 3 are referring to the dimensionalities of the acceleration in the perpendicular direction and local velocity, respectively. Following Ref. [47], half of the square of the corresponding mean angle [Fig. 7(a)] is used to normalize the probability density functions. The PDFs indeed obey the $F_{2,3}$ distribution in a fairly good way, especially for short time lags (solid color lines). For long time lags (dashed color lines), the normalized PDFs are deviating from the Fisher distribution as expected. This is because the long-time behavior is determined mainly by the geometry and is not influenced by the flow properties.

E. A Monte Carlo stochastic model

A Monte Carlo-based stochastic model to predict the long-time behavior of the curvature angle in the porous bed is developed and its prediction is compared with the asymptotic value obtained from the Lagrangian particle tracking in DNS. It is hypothesized that this long-time behavior of the curvature angle is dependent on the pore geometry. To verify such hypothesis, fluid trajectories are firstly modeled using the so-called "blocks" [see Fig. 9(a), three sample blocks in different colors are placed in a unit sphere]. Each block is generated by three points in space: one is the center of the sphere (O) and the other two (A and B) are on the surface. Accordingly, an angle (θ_S) is determined by those three points, which is used to mimic the curvature angle (Θ) along a real fluid trajectory. The cosine of this angle is defined as

$$\cos(\theta_S) = \frac{\overrightarrow{AO} \cdot \overrightarrow{OB}}{|\overrightarrow{AO}| \cdot |\overrightarrow{OB}|}. \tag{18}$$

In total 111 556 blocks are generated in the unit sphere so that it contains almost all possible angles ranging from 0 to π. The unit spheres with different sizes are then randomly placed and tested in the porous geometry [Fig. 9(b)]. Only the blocks that are in the fluid domain without any intersection with the solid beads are valid, indicating that the associated curvature angle may be possible in such

(a)

(b)

Sample filter function with three sets of blocks.

Filter functions with different sizes are randomly placed and tested in the 2D periodic channel.
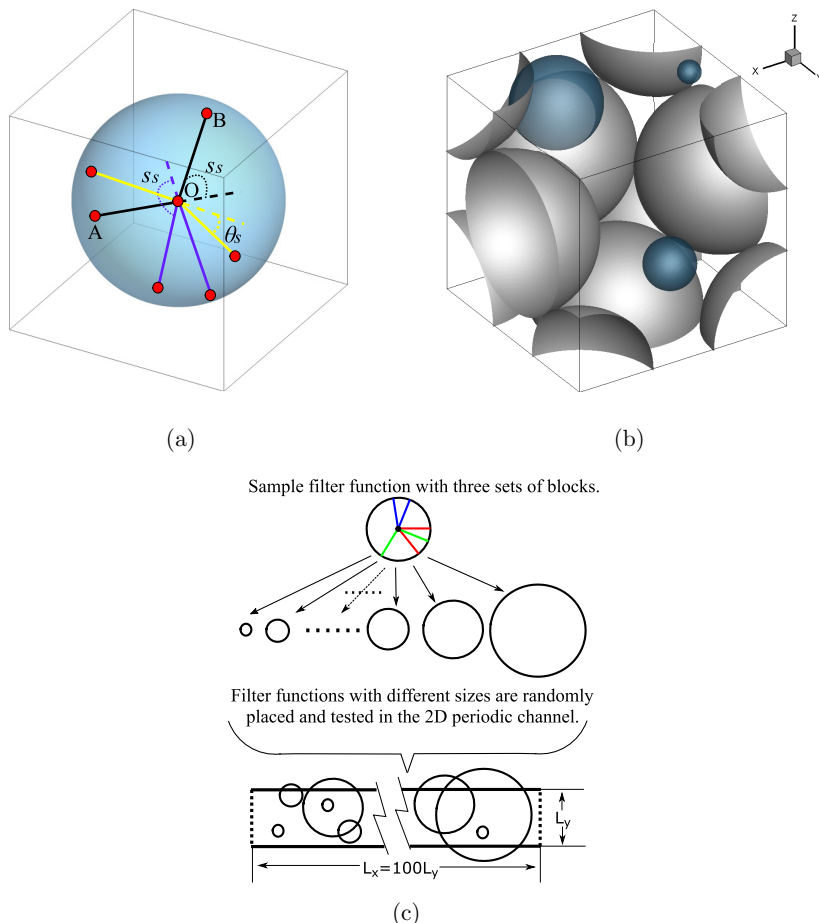
L_y

$L_x = 100 L_y$

(c)

FIG. 9. (a) Schematic of sample blocks in a mask function, (b) illustration of how the blue mask functions are placed inside of the porous bed, (c) application of the stochastic model to a two-dimensional periodic channel and corresponding two-dimensional mask functions denoted by circles of different radii.

scenario. This procedure is repeated to obtain a large number of samples (100 000 samples). The cosine of the angle is recorded for each valid realization and the mean value is calculated. The steps in the stochastic model are summarized as follows:

(i) The blocks in a unit sphere are constructed first. Three points A, B, and O [Fig. 9(a)] are used to compose one pair of block, where A and B are on the surface of the sphere, and O denotes the center. Over 100 000 blocks are built in the unit sphere and the cosine of the corresponding angles are in almost equal distribution;

(ii) Multiple spheres with sizes from 0.025 D_H to 5 D_H are then generated based on the unit sphere containing all the blocks. D_H represents the hydraulic diameter of the porous media and is defined as

$$D_H = D_B \frac{\phi}{1 - \phi}. \tag{19}$$

After that, these spheres are randomly placed and tested in the porous geometry;

(iii) To determine if one block is valid or not, a multistep geometric check is conducted to make sure there is no intersection between the block and the solid beads. Also, the periodicity is enforced during this procedure;

(iv) If one block has been verified to be valid, the associated cosine of the angle is recorded and counted into the final statistic. In total, 100 000 successful blocks are collected;

(v) To ensure the number of blocks is sufficient in this study, a convergence study is carried out with number of blocks of 66 564 and 272 484, which shows little impact of the block numbers on the final result. The deviation of the predicted asymptotic curvature angle between each case is below 0.2%.

The Monte Carlo-based stochastic model is first tested on a simple two-dimensional periodic channel with length (L_x) to be 100 times the width (L_y) and periodic boundary condition specified in the x direction. Similar to the three-dimensional case, a sample filter function or the mask function, containing three sample blocks illustrated by red, blue, and green colors, is displayed in Fig. 9(c). The filter function is designed to contain all the possible angles formed by three points. One of them is the center of the circle, and the other two points are selected randomly on a unit circle. Filter functions of different sizes [Fig. 9(c)] are then randomly placed into the test geometry (2D periodic channel) with the periodicity applied in the x direction. If any part of the block is interrupted by the solid boundary of the channel, this block is deemed invalid and not counted into the final statistic of the mean curvature of particle trajectories. Otherwise, the angle associated with the valid block is collected into the statistics. Over 200 000 filter functions were tested with about 100 000 blocks of different angles.

1. Two-dimensional, periodic channel

This simple two-dimensional case is selected to illustrate the effectiveness of this model, and also verify its appropriateness. For the periodic channel, more particle trajectories will be aligned in the axial flow direction owing to the confinement effect of the channel walls. This can be easily tested by varying the size of the mask/filter function from a very small radius of the circle to a much larger value compared to the width of the channel. The model is first applied to this simple test case, to understand the effect of confinement in two dimensions.

Intuitively, when the size of the filter function is small compared to the channel width, all blocks would have high probability to be valid; however, with increasing filter size, more blocks would become invalid owing to the confinement effect of the solid channel wall. In other words, when the diameter of the mask functions is small, the ensemble-averaged angle should be approaching $\pi/2$ indicating equidistribution of particle trajectories, that is, the confinement has little effect on the curvature angle. Whereas as the filter functions get larger compared to the channel width, because of the geometric confinement, the curvature angles are forced to get closer to either of the two extreme values, 0 or π. Therefore, at this moment $\langle\theta_S\rangle$ would again approach $\pi/2$. Moreover, when the filter sizes are in between (medium sized radii), a maximum of the averaged angle should be expected. This is because, larger angle blocks tend to have higher probability of being valid due to the effect of the confinement. It can be easily understood by imagining fluid particles hitting a solid wall. The particle would bounce back instead of penetrating through the wall. Thus, a large deflection angle is generated, which is essentially the defined curvature angle. As a result, a maximum value of the ensemble averaged curvature angle should be expected for a medium size filter function.

These intuitive understandings can be confirmed in Fig. 10, where the ensemble averaged curvature angle $\langle\theta_S\rangle$ is plotted against the diameter of the filter function (D_S) normalized by the width of the channel. The curvature angles for the mask functions with the smallest and largest sizes are indeed approaching $\pi/2$. And a peak was indeed observed in between.

2. Three-dimensional, triple periodic porous unit cell

The stochastic model is designed to test the mask functions with sizes from $D_S/D_H \approx 0.025$ to $D_S/D_H \approx 5$, when the filter function is about as the same size as the porous unit cell. The reasons for such a setting are explained in the following. First, the smallest size of the mask function ($D_S/D_H \approx 0.025$) is chosen to make the confinement effect almost negligible so that all the angles ought to have equal possibilities. And this is consistent with what is observed from Fig. 11. Second,
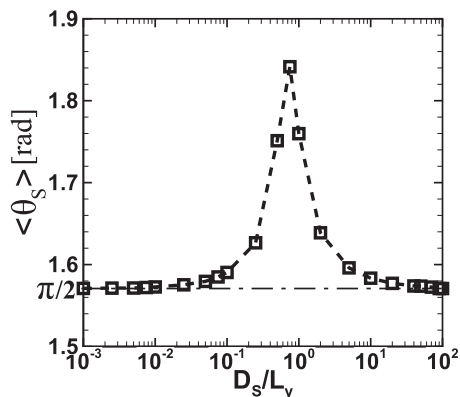
FIG. 10. Two-dimensional periodic channel: ensemble averaged curvature angle $\langle\theta_S\rangle$ as a function of mask function diameter D_S normalized by the channel width L_y.

if the size of the filter function exceeds the porous unit cell, the stochastic model may not be relevant. Due to the extreme compactness of the bed, the void space between each pore is connected in a meandering way. That is to say, almost no blocks are valid under this circumstance, and there is no physical meaning of using the size of the mask function larger than the porous unit cell. Besides, in the real scenario, the flow structures tend to be restricted inside of a single pore and thus restricting to mask functions smaller than the size of the unit cell is appropriate.

Figure 11 shows the ensemble averaged angle $\langle\theta_S\rangle$ computed from the stochastic model for different diameters, D_S, of mask functions, where D_S is normalized with D_H. It can be seen that the mean angle starts with $\pi/2$ with very small diameter, indicating all directions in the three-dimensional domain are equally probable for small size masking functions. The geometric confinement does not have any effect on the curvature angle at this point. After that, $\langle\theta_S\rangle$ increases with lager D_S, meaning the solid boundary of the beads is starting to limit the possibilities of valid blocks. This also means that the larger angles would have higher probabilities than the smaller angles. Then it reaches the maximum angle to be 1.724 radian at about $D_S/D_H = 2$, which implies that now the porous geometry has the greatest influence on the trajectories of the fluid. This influence can be qualitatively measured by the possibility of filter functions in contact with sphere boundaries. In other words, the more filter functions are interrupted by the beads, the higher impact confinement
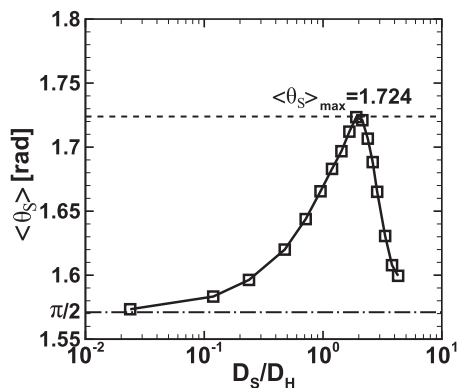

FIG. 11. Three-dimensional, triple periodic porous unit cell: ensemble averaged curvature angle θ_S as a function of mask function radius D_S normalized by the hydraulic diameter D_H.

can make to the fluid trajectories. At this moment, the porous geometry is playing the most important role. Reference [47] reported a different value ($\frac{2}{3}\pi$) for a two-dimensional confined domains (circle, rectangles of different aspect ratio), suggesting this maximum angle is geometric dependent. After it hits the maximum, $\langle\theta_S\rangle$ starts to decrease, resulting from that the pore size is limiting the angle of the blocks. That is to say, with the larger filter function sizes, some trajectory angles are preferred because of the limited pore size. This is the reason why the mean angle $\langle\theta_S\rangle$ decreases.

More importantly, it is confirmed that the maximum mean angle, $\langle\theta_S\rangle_{\max} = 1.724$ radian, is very close to the asymptotic limit of the mean absolute angle, $\theta(\tau \to \infty) = 1.72$ radian, obtained at large time lags for particles advanced by fluctuating fluid velocity only, as shown in Fig. 7(a). Such a good agreement comes from the fact that the stochastic model does not consider the influence of the mean flow. In other words, the mean angle is solely dependent on the pore geometry. Hence, matching of the asymptotic angle obtained from the fluctuation velocity field is to be expected. Again, that this value is different from $\pi/2$, as observed in isotropic turbulence, indicates the confinement effect of porous geometry on the flow structures.

V. SUMMARY AND CONCLUSION

Fully resolved direct numerical simulations were performed on a face-centered porous unit cell using a Cartesian grid-based fictitious domain method for three different pore Reynolds numbers of 300, 500, and 1000 spanning an unsteady transitional to fully turbulent flow. Flow physics in the Eulerian frame were explored and discussed first. Emphasis was then placed on multiscale, Lagrangian statistics of fluid flow as turbulent dispersive transport and mixing are easier to understand in a Lagrangian frame.

The flow field was visualized by the contours of the mean velocity and turbulent kinetic energy distributions. It is observed that the mean velocity field, i.e., the large-scale motion, keeps the same distribution regardless of Reynolds number; while the generation of TKE, representing the small-scale motions, is greatly enlarged and its distribution is noticeably altered. In addition, the spatial variances and probability density functions for the instantaneous and temporal fluctuation velocities were computed. The variances for the fluctuating velocities have larger values than those for the instantaneous velocities due to the stronger inertial effects. A reasonable agreement is found comparing the variances for the instantaneous velocities at $\text{Re}_p = 300$ with Ref. [22]. For higher Reynolds numbers, similar trends as in the literature are observed. However, a Reynolds number dependency was noticed for the decay rate of the PDF for the instantaneous velocities after three standard deviations. This is specific for the high Reynolds number cases and was not observed by Hill and Koch [22] at lower Re. This is attributed to the strong inertial influences at higher Re.

The Lagrangian auto-correlations were obtained by tracking a large number of fluid particle trajectories. It is found that the correlation in the streamwise direction decorrelates at about four times of the integral timescales regardless of the Reynolds numbers studied. The integral timescales in the spanwise directions are much smaller than that in streamwise direction. Moreover, the integral timescales in all directions decrease dramatically with increasing Reynolds number. The Lagrangian energy spectra were calculated by performing the Fourier transform on the auto-correlations. Even for the highest Re_p flow studied here, a power law with an exponent of -2, representing the inertial flow regime, was observed only in a very small region. Moreover, a pronounced f^{-1} trend is followed for higher frequencies. It is anticipated that the Reynolds number studied here is not high enough to obtain the inertial scaling in the Lagrangian energy spectrum.

Instantaneous multiscale curvature angles formed by three points with equal time-increments along a Lagrangian tracer trajectory were computed. The evolution of the mean angle, depending on time lags, was determined by ensemble averaging of the instantaneous angles. Two power laws were observed in the evolution. For short time lags, a linear relationship was found, indicating its dependency on the curvature of the trajectory. The inertial regime was noticeably pronounced with a trend with respect to the square root of the time lag at intermediate time lags. While at long time lags, an asymptotic behavior appeared to be 1.72 radian, different from $\pi/2$ observed for the

three-dimensional isotropic turbulence field [46] and $\frac{2}{3}\pi$ for the two-dimensional wall-bounded turbulent flow [47], representing equidistribution of the angle and the confinement effect on the flow structures, respectively. Consequently, the asymptotic value is conjectured to be geometry dependent. This shows that multiscale angular statistics yield scaling information for quantifying turbulence in a confined porous geometry requiring Lagrangian particle positions only.

The probability density functions for the cosine of the instantaneous curvature angles were predicted as well. A spike near the $\cos(\Theta) = 1$ for short time increments and an equidistribution for large time lags was detected. After appropriate normalization, the PDFs were fit to a Fisher distribution. The normalized PDFs for short time lags follow the $F_{2,3}$ distribution in a fairly good way, while those for long time lags deviate from it. This results from the fact that the long-time behavior of the PDFs is decided by the geometry instead of the flow field.

Finally, a Monte Carlo-based stochastic model to predict the long-time behavior of the mean absolute angle was developed. Filter functions with different blocks representing the possible curvature angles were constructed and tested inside of the porous bed. The predicted mean angle, evolving with increasing size of the filter functions, starts from $\pi/2$ meaning no confinement effect, increases to 1.72 radian representing maximum influence of the geometry, then decreases because of the limited pore size. This angle matching with the asymptotic curvature angle for the fluid particles moving with the instantaneous velocity fluctuations confirms the geometric confinement effect on the flow properties. The value of the maximum angle can be used to characterize different pore geometries and potentially provides an upper limit for angular statistics.

ACKNOWLEDGMENTS

[1] A. G. Dixon and M. Nijemeisland, CFD as a design tool for fixed-bed reactors, Ind. Eng. Chem. Res. **40**, 5246 (2001).

[2] R. Aris, *Elementary Chemical Reactor Analysis*, Prentice-Hall International Series in the Physical and Chemical Engineering Sciences (Prentice-Hall, Englewood Cliffs, NJ, 1969), p. 352.

[3] A. Shams, F. Roelofs, E. M. J. Komen, and E. Baglietto, Quasi-direct numerical simulation of a pebble bed configuration. Part I: Flow (velocity) field analysis, Nucl. Eng. Des. **263**, 473 (2013).

[4] D. Hlushkou and U. Tallarek, Transition from creeping via viscous-inertial to turbulent flow in fixed beds, J. Chromatogr. A **1126**, 70 (2006).

[5] A. Dybbs and R. V. Edwards, A new look at porous media mechanics—Darcy to turbulent, in *Fundamentals of Transport Phenomena in Porous Media*, edited by J. C. Bear and Y. Corapcioglu (Martinus Nijhoff Publishers, 1984), pp. 199–254.

[6] R. J. Hill, D. L. Koch, and A. J. C. Ladd, The first effects of fluid inertia on flows in ordered and random arrays of spheres, J. Fluid Mech. **448**, 213 (2001).

[7] T. Suekane, Y. Yokouchi, and S. Hirai, Inertial flow structures in a simple-packed bed of spheres, AIChE J. **49**, 10 (2003).

[8] R. Natarajan and A. Acrivos, The instability of the steady flow past spheres and disks, J. Fluid Mech. **254**, 323 (1993).

[9] G. I. Taylor, The criterion for turbulence in curved pipes, Proc. Roy. Soc. London A: Math. Phys. Eng. Sci. **124**, 243 (1929).

[10] A. J. Roberts, Shear dispersion along circular pipes is affected by bends, but the torsion of the pipe is negligible, SIAM J. Appl. Dynam. Syst. **3**, 433 (2004).

[11] T. H. Wegner, A. J. Karabelas, and T. J. Hanratty, Visual studies of flow in a regular array of spheres, Chem. Eng. Sci. **26**, 59 (1971).

[12] D. L. Koch and A. J. C. Ladd, Moderate Reynolds number flows through periodic and random arrays of aligned cylinders, J. Fluid Mech. **349**, 31 (1997).

[13] B. D. Wood, Inertial effects in dispersion in porous media, Water Resour. Res. **43**, 12 (2007).

[14] J. Finn, A numerical study of inertial flow features in moderate reynolds number flow through packed beds of spheres, Ph.D. dissertation, Oregon State University, 2013.

[15] P. Magnico, Hydrodynamic and transport properties of packed beds in small tube-to-sphere diameter ratio: Pore scale simulation using an Eulerian and a Lagrangian approach, Chem. Eng. Sci. **58**, 5005 (2003).

[16] M. A. Latifi, N. Midoux, A. Storck, and J. N. Gence, The use of micro-electrodes in the study of the flow regimes in a packed bed reactor with single phase liquid flow, Chem. Eng. Sci. **44**, 2501 (1989).

[17] H. S. Mickley, K. A. Smith, and E. I. Korchak, Fluid flow in packed beds, Chem. Eng. Sci. **20**, 237 (1965).

[18] S. Rode, N. Midoux, M. A. Latifi, and A. Storck, Hydrodynamics and liquid–solid mass transfer mechanisms in packed beds operating in cocurrent gas–liquid downflow: An experimental study using electrochemical shear rate sensors, Chem. Eng. Sci. **49**, 1383 (1994).

[19] D. Seguin, A. Montillet, and J. Comiti, Experimental characterisation of flow regimes in various porous media—I: Limit of laminar flow regime, Chem. Eng. Sci. **53**, 3751 (1998).

[20] D. Seguin, A. Montillet, J. Comiti, and F. Huet, Experimental characterization of flow regimes in various porous media—II: Transition to turbulent regime, Chem. Eng. Sci. **53**, 3897 (1998).

[21] D. F. Van der Merwe and W. H. Gauvin, Velocity and turbulence measurements of air flow through a packed bed, AIChE J. **17**, 519 (1971).

[22] R. J. Hill and D. L. Koch, The transition from steady to weakly turbulent flow in a close-packed ordered array of spheres, J. Fluid Mech. **465**, 59 (2002).

[23] V. A. Patil and J. A. Liburdy, Flow structures and their contribution to turbulent dispersion in a randomly packed porous bed based on particle image velocimetry measurements, Phys. Fluids **25**, 24 (2013).

[24] V. A. Patil and J. A. Liburdy, Scale estimation for turbulent flows in porous media, Chem. Eng. Sci. **123**, 231 (2015).

[25] A. R. Evseev, Visual study of turbulent filtration in porous media, J. Porous Media **20**, 549 (2017).

[26] J. Finn and S. V. Apte, Relative performance of body fitted and fictitious domain simulations of flow through fixed packed beds of spheres, Int. J. Multiphase Flow **56**, 54 (2013).

[27] M. F. Uth, Y. Jin, A. V. Kuznetsov, and H. Herwig, A direct numerical simulation study on the possibility of macroscopic turbulence in porous media: Effects of different solid matrix geometries, solid boundaries, and two porosity scales, Phys. Fluids **28**, 065101 (2016).

[28] Y. Jin, M. F. Uth, A. V. Kuznetsov, and H. Herwig, Numerical investigation of the possibility of macroscopic turbulence in porous media: A direct numerical simulation study, J. Fluid Mech. **766**, 76 (2015).

[29] P. Andrigo, R. Bagatin, and G. Pagani, Fixed bed reactors, Catal. Today **52**, 197 (1999).

[30] G. Eigenberger and W. Ruppel, *Catalytic Fixed-Bed Reactors* (Wiley Online Library, 2012).

[31] M. H. J. Pedras and M. J. S. de Lemos, Macroscopic turbulence modeling for incompressible flow through undeformable porous media, Int. J. Heat Mass Transf. **44**, 1081 (2001).

[32] J. R. A. Pearson and P. M. J. Tardy, Models for flow of non-Newtonian and complex fluids through porous media, J. Non-Newtonian Fluid Mech. **102**, 447 (2002).

[33] B. V. Antohe and J. L. Lage, A general two-equation macroscopic turbulence model for incompressible flow in porous media, Int. J. Heat Mass Transf. **40**, 3013 (1997).

[34] T. Masuoka and Y. Takatsu, Turbulence model for flow through porous media, Int. J. Heat Mass Transf. **39**, 2803 (1996).

[35] A. Nakayama and F. Kuwahara, A macroscopic turbulence model for flow in a porous medium, Trans. ASME: J. Fluids Eng. **121**, 427 (1999).

[36] K. Suga, Understanding and modeling turbulence over and inside porous media, Flow Turbul. Combust. **96**, 717 (2016).

[37] M. J. S. de Lemos and M. H. J. Pedras, Recent mathematical models for turbulent flow in saturated rigid porous media, Trans. ASME: J. Fluids Eng. **123**, 935 (2001).

[38] S. Pope, *Turbulent Flows* (Cambridge University Press, Cambridge, 2000).

[39] X. He, S. Apte, K. Schneider, B. Kadoch, and M. Farge, Turbulence and inertial effects in a porous bed: DNS and flow analysis, in *Proceedings of the Summer Program 2016, Center for Turbulence Research* (Stanford University, 2016), pp. 63–72.

[40] C. Hutter, A. Zenklusen, S. Kuhn, and P. R. von Rohr, Large eddy simulation of flow through a streamwise-periodic structure, Chem. Eng. Sci. **66**, 519 (2011).

[41] P. K. Yeung, Lagrangian investigations of turbulence, Annu. Rev. Fluid Mech. **34**, 115 (2002).

[42] H. Xu, N. T. Ouellette, and E. Bodenschatz, Curvature of Lagrangian trajectories in turbulence, Phys. Rev. Lett. **98**, 050201 (2007).

[43] B. Kadoch, D. del Castillo-Negrete, W. J. T. Bos, and K. Schneider, Lagrangian statistics and flow topology in forced two-dimensional turbulence, Phys. Rev. E **83**, 036314 (2011).

[44] A. Scagliarini, Geometric properties of particle trajectories in turbulent flows, J. Turbul. **12**, N25 (2011).

[45] P. Schaefer, Curvature statistics of streamlines in various turbulent flows, J. Turbul. **13**, N28 (2012).

[46] W. J. T. Bos, B. Kadoch, and K. Schneider, Angular Statistics of Lagrangian Trajectories in Turbulence, Phys. Rev. Lett. **114**, 214502 (2015).

[47] B. Kadoch, W. J. T. Bos, and K. Schneider, Directional change of fluid particles in two-dimensional turbulence and of football players, Phys. Rev. Fluids **2**, 12 (2017).

[48] S. V. Apte, M. Martin, and N. A. Patankar, A numerical method for fully resolved simulation (FRS) of rigid particle-flow interactions in complex flows, J. Comput. Phys. **228**, 2712 (2009).

[49] B. D. Wood, S. V. Apte, J. A. Liburdy, R. M. Ziazi, X. He, J. R. Finn, and V. A. Patil, A comparison of measured and modeled velocity fields for a laminar flow in a porous medium, Adv. Water Resour. **85**, 45 (2015).

[50] J. Finn and S. V. Apte, Integrated computation of finite-time Lyapunov exponent fields during direct numerical simulation of unsteady flows, Chaos **23**, 013145 (2013).

[51] P. R. Gunjal, V. V. Ranade, and R. V. Chaudhari, Computational study of a single-phase flow in packed beds of spheres, AIChE J. **51**, 365 (2005).

[52] G. I. Taylor, *Diffusion by Continuous Movements* (Proc. London Math. Soc, 1921), Vol. 1, p. 196.

[53] A. S. Monin and A. M. Yaglom, *Statistical Fluid Mechanics: Mechanics of Turbulence* (MIT Press, Cambridge, MA, 1965).

[54] S. Corrsin, Estimate of the relations between Eulerian and Lagrangian scales in large Reynolds number turbulence, J. Atmos. Sci. **20**, 115 (1963).